Geophysical Journal International

Geophys. J. Int. (2015) **201,** 459–474
GJI Seismology

doi: 10.1093/gji/ggv038

Scattering of high-frequency seismic waves caused by irregular surface topography and small-scale velocity inhomogeneity

Shunsuke Takemura,[1] Takashi Furumura[2,3] and Takuto Maeda[2]

[1] *Department of Material System Science, Graduate School of Nanobioscience, Yokohama City University,* 22-2 *Seto, Kanazawa-ku, Yokohama* 236-0027, *Japan. E-mail: shunsuke@yokohama-cu.ac.jp*
[2] *Earthquake Research Institute, The University of Tokyo,* 1-1-1 *Yayoi, Bunkyo-ku, Tokyo* 113-0032, *Japan*
[3] *Center for Integrated Disaster Information Research, Interfaculty Initiative in Information Studies, The University of Tokyo,* 7-3-1 *Hongo, Bunkyo-ku, Tokyo* 113-0033, *Japan*

Accepted 2015 January 19. Received 2015 January 19; in original form 2014 June 4

SUMMARY

Based on 3-D finite difference method simulations of seismic wave propagation, we examined the processes by which the complex, scattered high-frequency ($f > 1$ Hz) seismic wavefield during crustal earthquakes is developed due to heterogeneous structure, which includes small-scale velocity inhomogeneity in subsurface structure and irregular surface topography on the surface, and compared with observations from dense seismic networks in southwestern Japan. The simulations showed the process by which seismic wave scattering in the heterogeneous structure develops long-duration coda waves and distorts the *P*-wave polarization and apparent *S*-wave radiation pattern. The simulations revealed that scattering due to irregular topography is significant only near the station and thus the topographic scattering effects do not accumulate as seismic waves propagate over long distances. On the other hand, scattering due to velocity inhomogeneity in the subsurface structure distorts the seismic wavefield gradually as seismic waves propagate. The composite model, including both irregular topography and velocity inhomogeneity, showed the combined effects. Furthermore, by introducing irregular topography, the effects of seismic wave scattering on both body and coda waves were stronger than in the model with velocity inhomogeneity alone. Therefore, to model the high-frequency seismic wavefield, both topography and velocity inhomogeneity in the subsurface structure should be taken into account in the simulation model. By comparing observations with the simulations including topography, we determined that the most preferable small-scale velocity heterogeneity model for southwestern Japan is characterized by the von Kármán power spectral density function with correlation distance $a = 5$ km, rms value of fluctuation $\varepsilon = 0.07$ and decay order $\kappa = 0.5$. We also demonstrated that the relative contribution of scattering due to the topography of southwestern Japan is approximately 12 per cent.

Key words: Earthquake ground motions; Body waves; Computational seismology; Wave scattering and diffraction; Wave propagation.

1 INTRODUCTION

High-frequency ($f > 1$ Hz) seismograms show completely different features compared to those of low-frequency ($f < 1$ Hz) seismograms due to seismic wave scattering of short-wavelength components during propagation in heterogeneous structure. Heterogeneities in the Earth, which especially cause seismic wave scattering of high-frequency seismic waves, are formed by small-scale velocity inhomogeneity in the subsurface structure and irregular topography on the surface, which have characteristic scales shorter than several kilometres. Complex features of the scattered high-frequency seismic wavefield can be noticed in the seismograms. These features include those from the broadening of *P*- and *S*-wave pulses (e.g. Sato 1989; Saito *et al.* 2005; Takahashi *et al.* 2007), distortion of the apparent *S*-wave radiation pattern from the original four-lobe source radiation pattern (e.g. Liu & Helmberger 1985; Takemura *et al.* 2009; Sawazaki *et al.* 2011), the appearance of *P*-wave energy in transverse motion (e.g. Kubanza *et al.* 2007; Nishimura 2012; Takemura & Furumura 2013) and the excitation of long-duration coda waves (e.g. Aki & Chouet 1975; Sato 1984). Previous studies on the scattered high-frequency seismic wavefield were often examined based on numerical approaches

(e.g. Ohminato & Chouet 1997; Nielsen *et al.* 2003; Ripperger *et al.* 2003; O'Brien & Bean 2009; Takemura *et al.* 2009; Kumagai *et al.* 2011; Imperatori & Mai 2013; Takemura & Furumura 2013) and theoretical experiments using the Markov and Born approximation theories (e.g. Saito *et al.* 2005; Przybilla *et al.* 2009; Takahashi *et al.* 2009), assuming either the effect of topography or the effect of velocity inhomogeneity in isolation. Furthermore, since surface topography should have a much stronger effect on surface waves rather than body waves since surface wave propagates long distances along the free surface, surface wave scattering due to topography has been studied extensively (e.g. Maradudin *et al.* 1991; Mayer *et al.* 1991; Köhler *et al.* 2012; Capdeville & Marigo 2013). Recently, Kumagai *et al.* (2011) pointed out that the effects of scattering of high-frequency body waves due to the complex topographic changes in volcanic areas are sufficiently strong compared with those of scattering due to structural velocity heterogeneities. However, it still remains uncertain how irregular topography and structural heterogeneity modify the seismic wavefield and develop the observed complex *P* and *S* waveforms.

In this study, we investigated the relative contributions of irregular topography and small-scale velocity inhomogeneity to the scattering of high-frequency seismic waves separately by 3-D finite difference method (FDM) simulations of seismic wave propagation using high-resolution surface topography and stochastic structural velocity inhomogeneity models of southwestern Japan. Through a set of simulations, we quantitatively examined the changes in the *P*-wave polarization and distortion of the apparent *S*-wave radiation pattern from the original four-lobe source radiation pattern. Snapshots of the *P* and *S* wavefields and synthetic seismograms of the different types of heterogeneous models demonstrated the detailed characteristics of the scattered high-frequency wavefield in the heterogeneous structure. The simulation results were compared with observed records of shallow crustal earthquakes from dense seismic networks (Hi-net, K-NET and KiK-net) operated by the National Research Institute for Earth Science and Disaster Prevention (NIED; Kinoshita 1998; Okada *et al.* 2004; Obara *et al.* 2005).

2 3-D FDM SIMULATION OF HIGH-FREQUENCY SEISMIC WAVEFIELDS

2.1 Simulation models

To demonstrate the process by which irregular topography and small-scale velocity inhomogeneity develop the scattered high-frequency seismic wavefield, we conducted 3-D FDM simulations of seismic wave propagation using irregular surface topography and heterogeneous velocity structure models. We chose the area of simulation in southwestern Japan, where the distribution of small-scale velocity inhomogeneities in the crust was well examined by comparison between observations and FDM simulations (e.g. Takemura *et al.* 2009; Takemura & Furumura 2013).

The area of the FDM simulation covered a zone of 128 km × 128 km in horizontal directions and 64 km in depth, which was discretized by grid intervals of 0.1 and 0.05 km in the horizontal (x, y) and vertical (z) directions, respectively. Elastic wave propagation at each gridpoint was calculated by solving equations of motion using a staggered-grid FDM with fourth-order and second-order in space and time, respectively. The zero-stress boundary condition of Okamoto & Takenaka (2005) was applied in the FDM simulation along the irregular surface to simulate the reflections of the high-frequency seismic waves from the irregular solid–air boundary as precisely as possible. Similar techniques have been applied in FDM simulations of seismic wave propagation in volcanic and oceanic areas (e.g. Ohminato & Chouet 1997; Ripperger *et al.* 2003; Nakamura *et al.* 2012), where strong topographic variations exist. The accuracy of the free-surface boundary condition for implementing irregular surface topography in the FDM based on the above scheme is examined in the Appendix A.

A high-resolution (50 m) digital elevation map (DEM) of southwestern Japan, provided by the Geographical Survey of Japan (GSJ), was used in the present the simulation (Fig. 1). The maximum height of the topography in the mountain region was 1200 m, and the maximum sea depth of the internal sea was −200 m. We adopted this high-resolution topography model in the simulation model with horizontal and vertical grid intervals of 0.1 and 0.05 km, respectively.

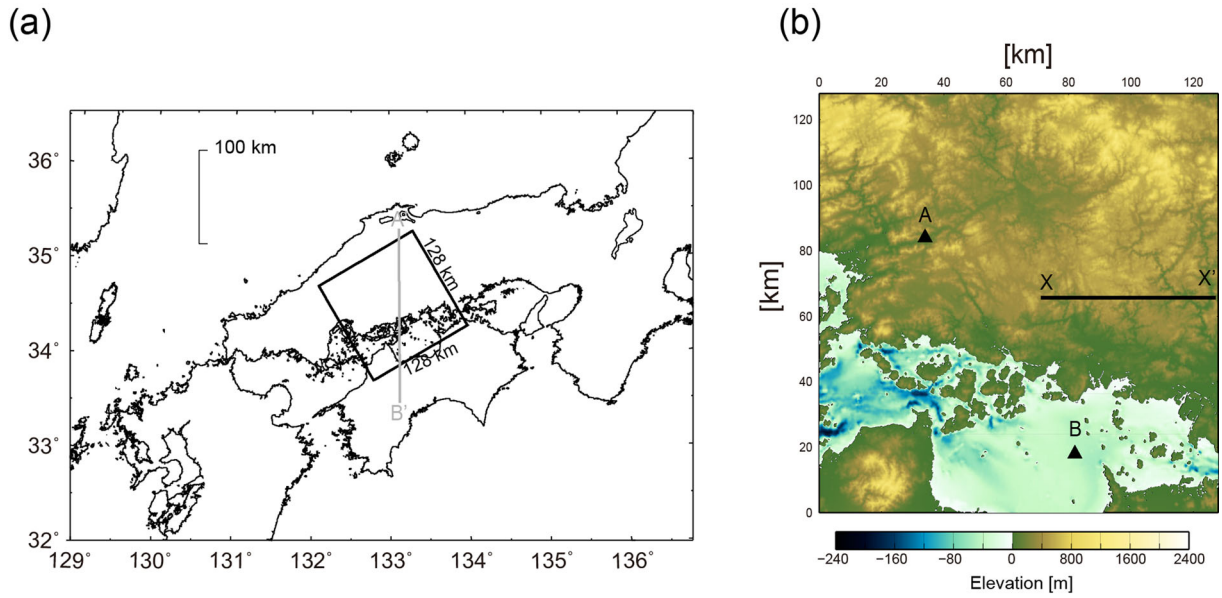

Figure 1. Topography model of the study area used for the 3-D simulation: Shikoku–Chugoku, southwestern Japan, showing (a) the area of the present 3-D simulation (black solid square) and the section of the 2-D calculation test (bold grey line) and (b) the distribution of surface elevation in metres.

The distribution of small-scale velocity inhomogeneity in the curst of southwestern Japan was referred from previous studies in this region (e.g. Takemura *et al.* 2009; Carcole & Sato 2010; Sawazaki *et al.* 2011; Takemura & Furumura 2013). These studies demonstrated that small-scale velocity heterogeneity in the crust and mantle could be described by the von Kármán power spectrum density function (PSDF; Sato *et al.* 2012) with correlation distance $a = 3$–5 km, rms value of fluctuation $\varepsilon = 0.03$–0.09 and $\kappa = 0.5$–0.8. Thus, we first assumed an isotropic stochastic random fluctuation model described by the von Kármán PSDF with correlation distance $a = 5$ km, rms value of fluctuation $\varepsilon = 0.05$ and decay order $\kappa = 0.5$. The stochastic random fluctuation was superposed on the background *P*- and *S*-wave velocity model for the crustal model of southwestern Japan with average velocities of $\langle V_P \rangle = 5.8$ km s^{-1} and $\langle V_S \rangle = 3.36$ km s^{-1}, respectively. In this simulation, we simply assumed a homogeneous half-space background velocity rather than a realistic velocity structure of actual Earth in order to compare the differences in the scattering seismic wavefields due to irregular topography and velocity inhomogeneity clearly and separately. We assumed an average density $\langle \rho \rangle = 2.6$ g cm^{-3} and correlated the relation between velocities and density fluctuations using Birch's law (Birch 1961). A frequency dependent Q^{-1} model developed by Robertsson (1994) was incorporated in the FDM simulation with $Q_P = 600$ and $Q_S = 300$ for *P* and *S* waves, respectively, and a central frequency $f_0 = 2$ Hz. With an averaged *S*-wave velocity (3.36 km s^{-1}) and grid size (0.1 km), the present FDM simulations could examine the scattered high-frequency wavefield at frequency below $f = 4.2$ Hz (wavelength $\lambda = 0.8$ km) with a sampling of 8 gridpoints per minimum *S* wavelength. Thus, we examined the scattering of seismic waves whose wavelengths are comparable or longer compared to the topographic difference in southwestern Japan.

The FDM simulations were conducted using the Earth Simulator supercomputer at the Japan Agency for Marine-Earth Science and Technology (JAMSTEC), which required computer memory of 389 GByte and a wall-clock time of 1.6 hr by parallel computing using 16 nodes (128 CPUs) of the supercomputer to evaluate seismic wave propagation of 40 s by 16 000 time-step calculations.

In this simulation, we examined seismograms at uniformly distributed virtual seismic stations at an interval of 1 km (16 384 stations) to obtain the statistical properties of the scattering high-frequency seismic wavefield by analysing a large number of simulation data.

2.2 Simulation of scattered *P* wavefield

First, we conducted FDM simulations of high-frequency *P*-wave propagation in the heterogeneous structures. We employed an explosive *P*-wave source at a depth of 5 km below the surface using a single-cycle Kupper wavelet source-time function (e.g. Mavroeidis & Papageorgiou 2003) with a moment release $M_0 = 1.26 \times 10^{15}$ Nm (M_w 4.0) and a dominant period of $T_0 = 0.16$ s, which radiated *P* waves isotropically over the simulation model, to examine the seismic wave propagation at frequency below $f = 4.2$ Hz stably. Since high-frequency surface wave excitation is very weak compared to scattered body waves in this setting (e.g. Sato *et al.* 2012), we mainly focused our attention on the scattering of body waves due to the heterogeneities.

The results of the FDM simulation are illustrated in Fig. 2 as a sequence of snapshots of the seismic *P* and *S* wavefields at $t = 3$, 6 and 12 s from the earthquake origin time. The contributions of the *P* and *S* waves at the surface, which were derived by calculating the divergence (compressional component) and rotation (shear component) from the 3-D wavefield, respectively, are shown in red and green, respectively. The snapshots compare the scattered wavefields derived from simulations of the irregular topography model (Fig. 2a), the velocity inhomogeneity model (Fig. 2b) and a composite model including both effects (Fig. 2c).

2.2.1 *Scattering due to irregular topography*

The first snapshot ($t = 3$ s) of the irregular topography model (Fig. 2a) shows spreading of the circular *P* wave front (red) and following strong scattered *P*-to-*S* converted signals (green), leading the long-duration coda waves at later time steps ($t = 6$, 12 s). It was confirmed that most of the scattered wavefield due to irregular topography is constructed by *P*-to-*S* conversion scattering, whereas *P*-to-*P* scattering is relatively weak, as already revealed by theoretical studies on seismic wave scattering in inhomogeneous velocity structure (e.g. Sato *et al.* 2012 chapter 4; Przybilla *et al.* 2006). At the middle time ($t = 6$ and 12 s in Fig. 2a), scattering of seismic waves is stronger in the mountain areas (upper part of the simulation area) than it in the sea (lower part), as expected by variation of the topography shown in Fig. 1. Furthermore, the later frame of the snapshot ($t = 12$ s) shows that the cylindrical shape of the *P* wave front is almost preserved after propagating more than 50 km in the irregular topography model, which indicates that for earlier part of *P* waves, the topographic scattering occurred only once when the direct *P* waves arrived at the surface and the distortion of the *P* wave front due to topographic scattering does not occur during propagation in the irregular topography model. Thus, we note that the topographic scattering is a localized (i.e. site-scale) phenomenon and is not an accumulating phenomenon during seismic wave propagation.

2.2.2 *Scattering due to velocity inhomogeneity*

The sequence of snapshots in Fig. 2(b) illustrates the scattered wavefield due to small-scale velocity inhomogeneity in the subsurface structure. In this simulation, we assumed a flat topography to exclude the topographic scattering effect. The simulation result demonstrates a remarkably distorted *P* wave front propagating in the heterogeneous structure, even in the early time frame of the snapshot ($t = 3$ s). The spread of the *P*-wave energy in model space by the scattering due to velocity inhomogeneity is clearly demonstrated with wider broadening of *P*-wave pulses, and this broadening effect becomes stronger with increasing distance. It is noteworthy that the effect of the scattering due to velocity inhomogeneity in the crust gradually accumulates with increasing propagation distance. Thus, the effects of seismic wave scattering in the heterogeneous subsurface structure accumulate with the propagation of seismic waves. On the other hand, the development of *S*-wave coda due to *P*-to-*S* conversion scattering is very weak compared with that in the topographic model (Figs 2a and b).

2.2.3 *Scattering in the composite heterogeneous model*

The snapshots derived from the simulation of the composite model (Fig. 2c) demonstrate the combination of the effects of both the irregular topography and velocity inhomogeneity scattering, which were shown in Figs 2(a) and (b). A significant distortion of the *P* wave front and following large and long-duration *S*-wave coda are shown in the wavefield. The scattered wavefield in the actual Earth

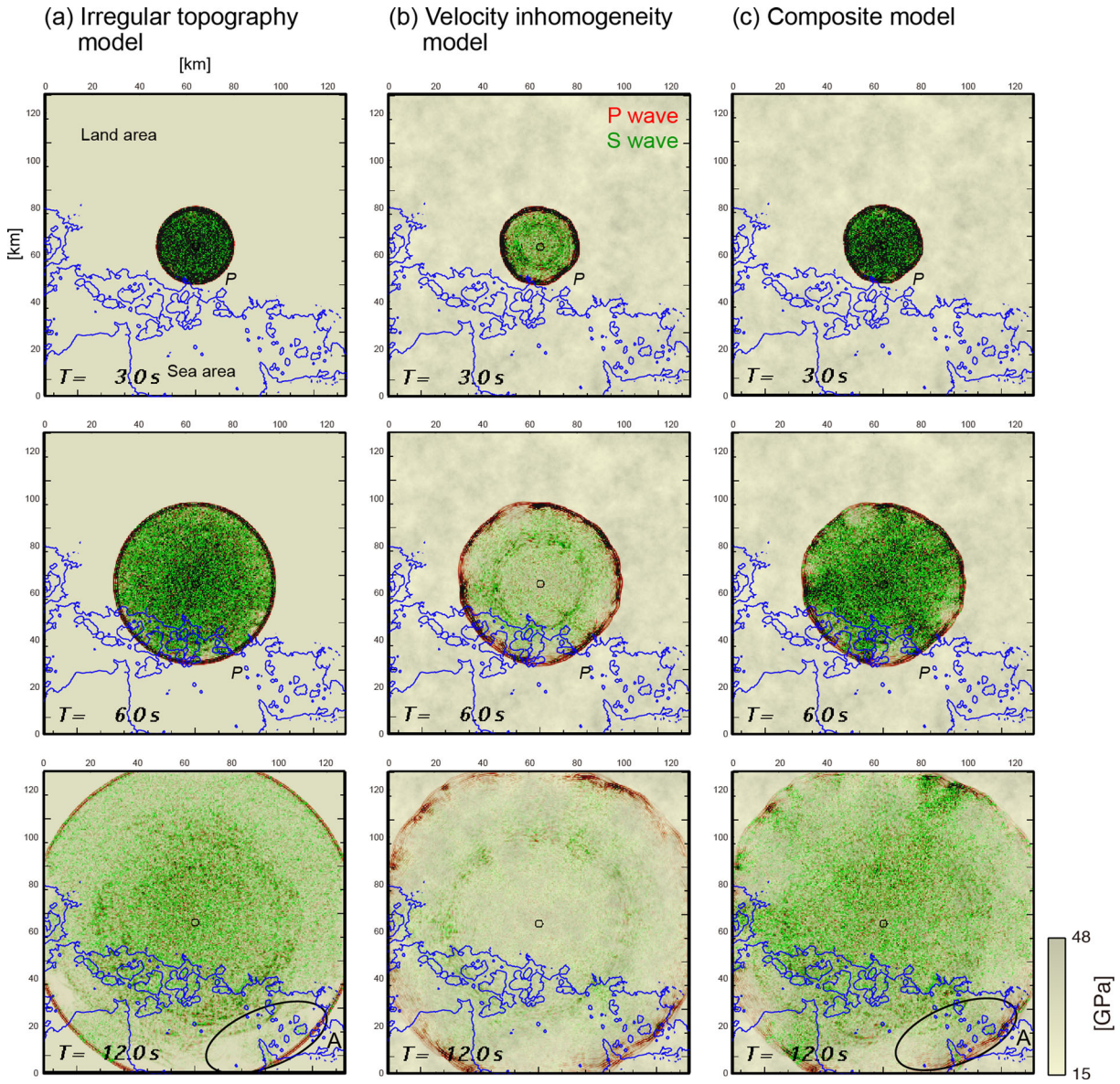

Figure 2. Snapshots of the seismic wavefield at the surface at $t = 3$, 8 and 12 s from the earthquake origin time showing P (red) and S (green) wave propagation derived from (a) the irregular topography model, (b) the velocity inhomogeneity model and (c) the composite model including both.

is considered to be developed by different mechanisms, such as irregular topography on the surface and velocity inhomogeneities in the subsurface structure. Although significant distortion of the initial P wave front developed by the scattering of P waves due to the velocity inhomogeneity (Fig. 2b), it is somewhat suppressed in the present simulation by introducing irregular topography. It is considered that the topographic scattering removes P-wave energy by conversion to S waves (see the $t = 12$ s frames).

2.2.4 *Record section of the scattered seismic waves*

The velocity seismograms of the transverse component derived by the simulations of the three models are shown in Fig. 3. Synthetic seismograms are recorded at stations aligned along the profile X–X′ in Fig. 1. We applied a bandpass filter for the frequency range of 1–4 Hz to each seismogram and multiplied by the hypocentral distance to compensate for geometrical spreading of the body waves. We note that the appearance of the P waves in the transverse component indicates that the polarization pattern is modified by reflection, refraction and scattering of the P waves due to the 3-D heterogeneous structure.

The record section of the irregular topography model (Fig. 3a) shows strong variation, such as in the amplitude of the direct P waves and the duration of the P-wave coda. This confirms our explanation that the topographic scattering is a localized effect, occurring at the station scale but not accumulating with propagation.

The record section of the velocity inhomogeneity model (Fig. 3b) shows a burst of large-amplitude P waves, which appear repeatedly over long distances with an interval of about 10–20 km. This repeating interval might be related to the correlation distance of the velocity inhomogeneity that we introduced into the simulation model ($a = 5$ km). We confirmed that the amplitude burst pattern would be changed dramatically with heterogeneities of different correlation distances ($a = 2$, 10 km; see Appendix B). The amplitude of the P waves of the transverse component increases gradually with propagation, developing a large and long-duration P-wave coda.

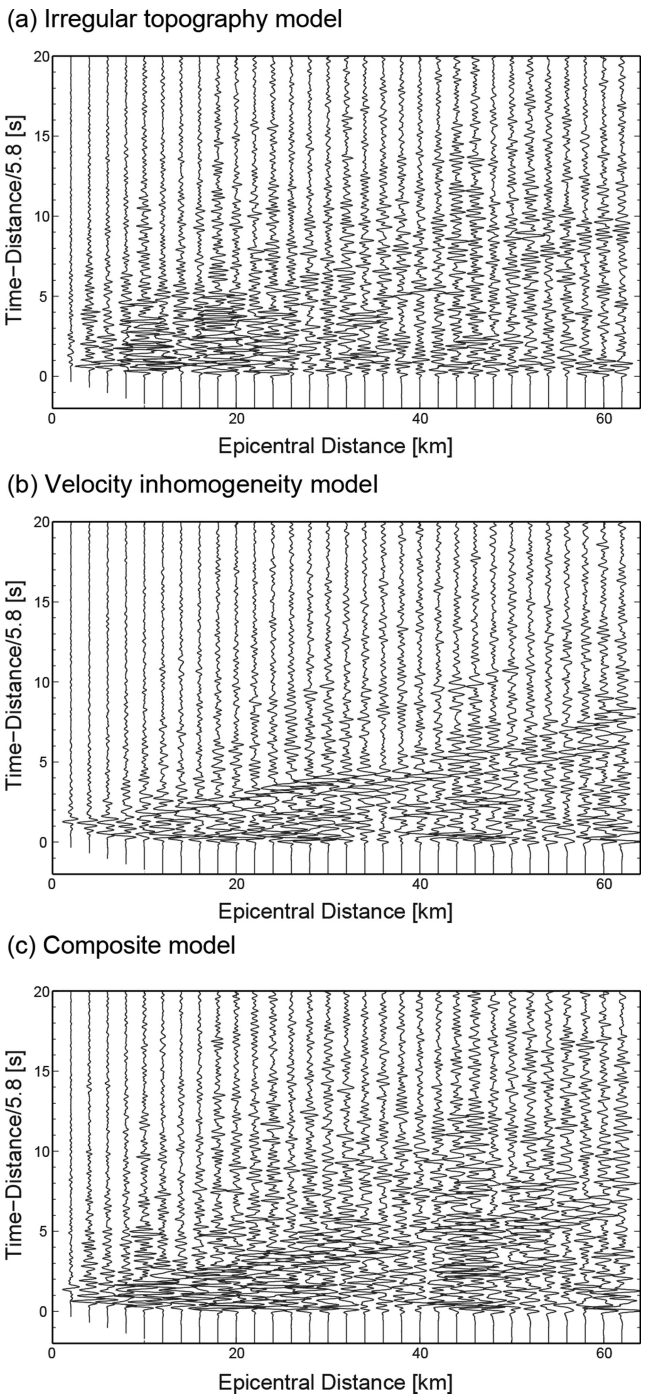

Figure 3. Synthetic seismograms of transverse-component ground velocity motion derived from the 3-D FDM simulation using (a) the irregular topography model, (b) the velocity inhomogeneity model and (c) the composite model including both. A bandpass filter for the frequency band of $f = 1$–4 Hz was applied. Each trace was multiplied by the hypocentral distance to compensate for geometrical spreading of body waves.

The record section of the composite model including both types of heterogeneities shows the large amplitude of the *P* wave and long-duration coda wave (Fig. 3c). The repeatable burst of the larger *P* wave due to the velocity inhomogeneity (Fig. 3b) has almost disappeared by overlapping with the long-duration large-amplitude scattered signals produced by the irregular topography. As a consequence, the combination of such different types of seismic wave scattering in the actual Earth homogenizes the spatial variation of the scattered wavefield.

2.2.5 *Waveform similarities between neighbouring stations*

In order to examine the scattering of seismic waves due to topographic and velocity heterogeneities in more detail, we calculated the cross-correlation coefficient (CCC) between waveforms of neighbouring stations. We applied a bandpass filter between 1 and 4 Hz to the *P* waveforms and calculated the CCC for the 5-s time window after the arrival of *P* wave. The estimated values of the CCC for radial-, transverse- and vertical-component seismograms are illustrated in Fig. 4 as a function of lag distances between stations. The estimation error of the CCC at each lag distance was evaluated based on the bootstrap method (Efron & Tibshirani 1986).

The CCC was shown to decrease gradually with increasing lag distance, a trend that is very strong for the *P* waveform in the transverse and vertical components but is rather gentle in the radial component. This occurred because the *P* wave in the transverse component is the scattering signal developed from the *P* wave in radial and vertical components. Additionally, it is considered that the polarization pattern of the *P* wave is very sensitive in vertical motion compared with radial motion because *P*-wave energy is almost polarized in the radial component in the case of a shallow earthquake through the homogeneous medium. The decrease of the CCC with increasing lag distance due to the scattering in irregular topography is much stronger than that caused by the velocity inhomogeneity, which shows a gradual decrease in CCC with lag distance.

It is interesting to note that the CCC for the transverse and vertical components shows its minimum value (0.05 for the transverse and 0.5 for the vertical component) at a lag distance of about 1 km but then recovers gradually with increasing lag distance to 2 km. We considered that the lag distance of minimum CCC correlates with the dominant correlation distances of topographic variations.

On the other hand, the velocity inhomogeneity model shows monochromatic decay in CCC with increasing lag distance. These experiments confirm our finding that the topographic scattering is a localized effect, simply modifying seismic waveforms around stations, while the scattering due to velocity inhomogeneity is a broad effect accumulating gradually along the propagation of seismic waves.

2.2.6 *Envelope of high-frequency seismograms*

Seismic coda waves are one of most important factors for measuring the strength of seismic wave scattering in the heterogeneous Earth (e.g. Aki & Chouet 1975; Sato *et al.* 2012, chapter 3). Thus, we compared the envelope shape of the coda wave for each heterogeneous model by calculating the mean square (MS) envelopes for the simulated waveforms at two stations, one located in the mountainous area (Fig. 5a; mark A in Fig. 1) and one in the sea area (Fig. 4b; mark B in Fig. 1).

For the station in the mountain area, most of the coda-wave amplitude for a sufficient amount of the later part (20–30 s) is developed due to topographic scattering (red line in Fig. 5a), and this portion is about 10 times larger than that caused by scattering due to velocity inhomogeneity (blue line in Fig. 5a). The strong temporal fluctuations in the coda amplitude, such as in the snapshots at 6, 15 and 24 s, are also developed by the topographic scattering effect. On the other hand, the amplitude of the coda envelope due to

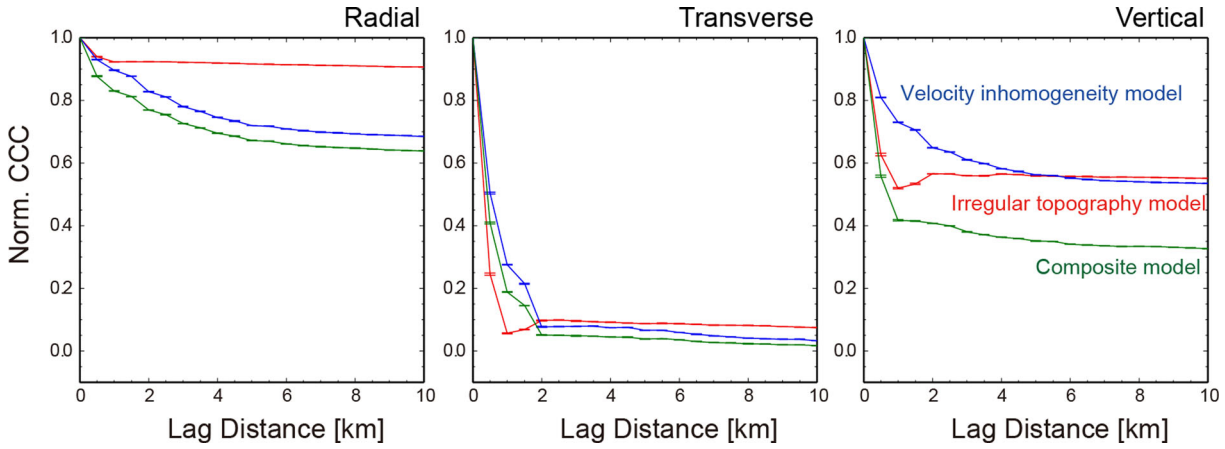

Figure 4. Change with distance in the cross-correlation coefficient (CCC) between station pairs: comparison between the irregular topography model, the velocity inhomogeneity model and the composite model. A bandpass filter for the frequency band of $f = 1$–4 Hz was applied. The cross-correlation coefficient was calculated by the *P* waveform for the 5-s time window that starts at *P*-wave arrival.

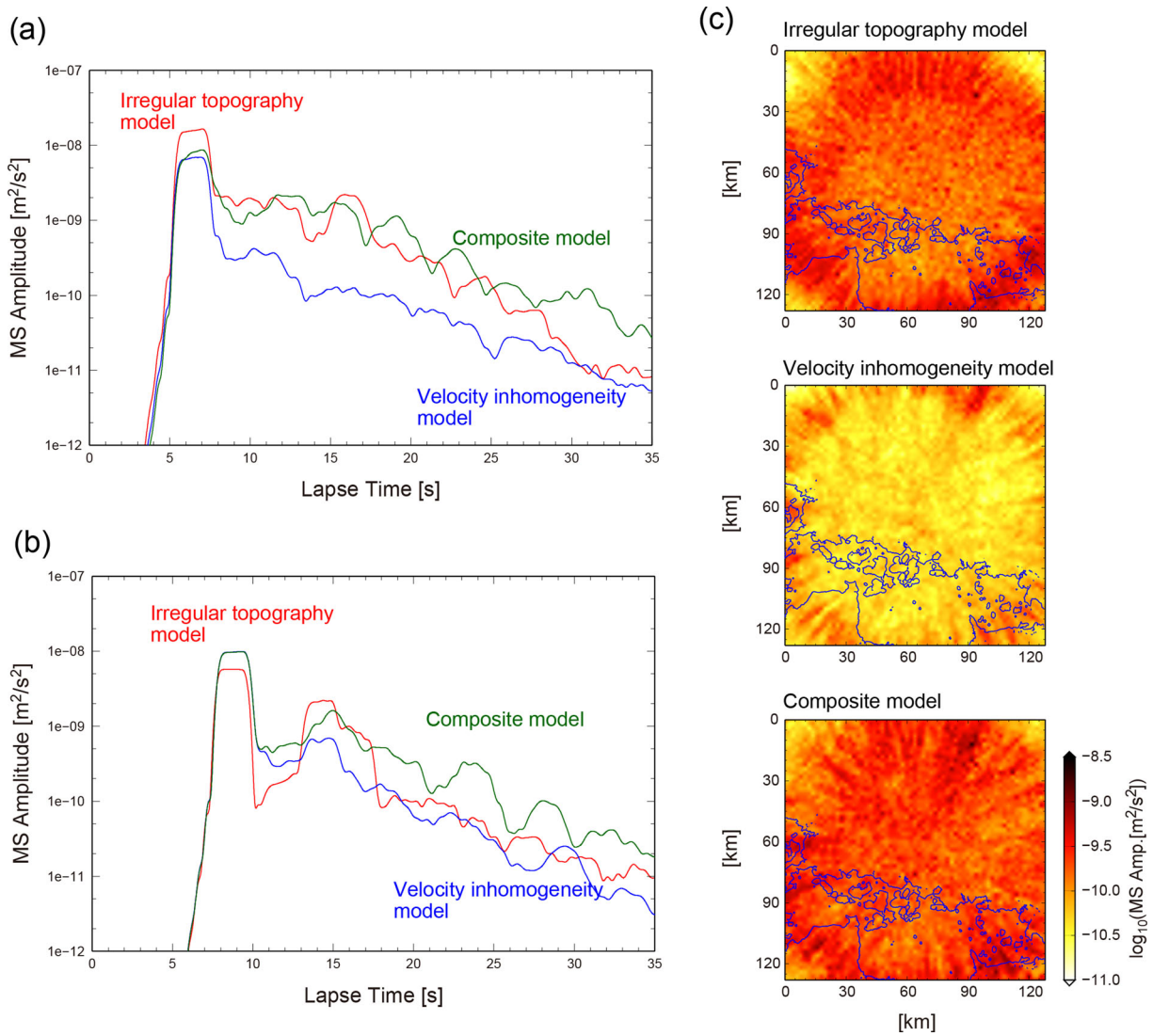

Figure 5. Mean-square (MS) envelopes of the bandpass-filtered three-component seismograms of each model recorded for (a) the mountain area and (b) the ocean region (stations A and B, respectively, in Fig. 1a). The epicentral distances of mountain and ocean stations are 36.4 and 49.6 km, respectively. Spatial variation of coda amplitude calculated for the 5-s time window between the lapse times of 20 and 25 s is shown in (c).

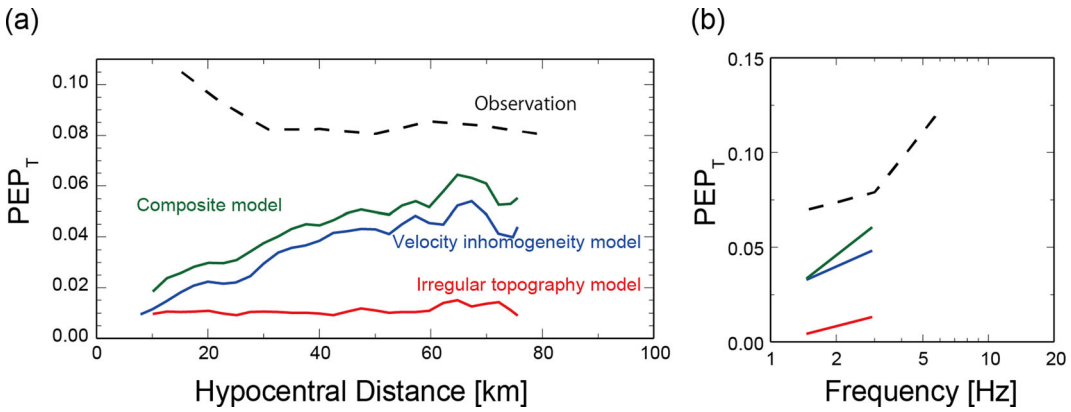

Figure 6. Changes in PEP_T as a function of hypocentral distance and frequency derived from simulation results using the irregular topography model (red line), the velocity inhomogeneity model (blue line) and the composite model including both velocity inhomogeneity and irregular topography (green line). The dashed line represents the observations of Takemura & Furumura (2013).

the velocity inhomogeneity model (blue line) decays smoothly with increasing time.

The strengths of the scatterings due to irregular topography and velocity inhomogeneity are roughly comparable for developing the coda at the ocean station (Fig. 5b), where the lateral variation of topography is relatively small, but the coda amplitude by scattering due to irregular topography in the mountain area is about 10 times larger than that by scattering due to velocity inhomogeneity. The composite model demonstrates that coda energies for the later part (>15 s) at both mountain and ocean are larger than those in the velocity inhomogeneity model.

Fig. 5(c) shows the spatial variation of the amplitude of *P*-wave coda generated by the simulations of the three models (Fig. 4c). The coda amplitudes were measured for a 5-s time window with a lapse time between of 20 and 25 s. Strong spatial variations of the coda amplitude are developed by the simulation of the irregular topography model, where the area of larger coda corresponds to the area of irregular topography (see Fig. 1b). On the other hand, the results of the simulations of other two models show an almost uniform distribution of coda amplitude.

2.2.7 *P-wave amplitude in transverse component*

We then examined the *P*-wave energy partition of the transverse component (hereafter denoted as PEP_T; see Takemura & Furumura 2013), which represents the relative strength of the *P*-wave energy of the transverse component developed by seismic wave scattering. We calculated the PEP_T using the initial *P*-wave part of each component envelope $e_i(t)$ (i = R, T and V) as

$$\mathrm{PEP_T} = \frac{\langle E_T \rangle}{\langle E_R \rangle + \langle E_T \rangle + \langle E_V \rangle},$$
$$\langle E_i \rangle = \frac{1}{T_W} \int_{TP-1}^{T_P+T_W-1} e_i(t)\,\mathrm{d}t, \qquad (1)$$

where T_P is the arrival time of *P* wave and T_W is the time window with $T_W = 3$ s. The subscripts R, T and V indicate the radial, transverse and vertical components, respectively. We note that for laterally homogeneous structure, no *P*-wave appears in the transverse component (i.e. $PEP_T = 0$); however, for heterogeneous structure, strong scattering equalizes the *P*-wave energy among the three components (i.e. $PEP_T = 1/3$). We took an average of the PEP_T for all directions at each distance or each frequency band.

The change in PEP_T as a function of hypocentral distance and frequency for the different heterogeneity models is shown in Fig. 6. The value of PEP_T increases linearly with increasing hypocentral distance from 10 to 50 km in the velocity inhomogeneity model with a maximum PEP_T of about 0.06 at epicentral distance of 65 km. The increase in PEP_T was stopped beyond this distance. On the other hand, the value of PEP_T in the irregular topography model (red line) is relatively small and almost constant (0.008–0.012), irrespective of hypocentral distance. These features are consistent with the findings shown in the snapshots (Figs 2a and 3a) that the topographic scattering shows only a localized effect at each site and that the effect does not accumulate with propagation of seismic waves. By comparing the results of the above simulation with dense Hi-net observations for shallow earthquakes that occurred in southwestern Japan (Takemura & Furumura 2013), it was confirmed that the relative strength of topographic scattering is expected to be approximately 12 per cent of the total strength of scattering of the high-frequency wavefield.

Fig. 6(b) compares the change in PEP_T as a function of frequency in epicentral distances of 50–60 km. It illustrates a linear increase in PEP_T with increasing frequency from $f = 1$ to 4 Hz for both the velocity inhomogeneity and irregular topography models, which is due to stronger seismic wave scattering for the high-frequency seismic wavefield with shorter wavelength.

The simulated PEP_T derived from the composite model (0.02–0.06) is somewhat smaller than the observed PEP_T (0.08–0.11; broken line in Fig. 6a). Thus, we conducted additional FDM simulation using the composite model but changing the parameter of velocity heterogeneity. Because of the trade-off between parameters, we simply changed the rms value of fluctuation ε (=0.03, 0.05, 0.07 and 0.09). Fig. 7 shows the changes in PEP_T for the frequency range of 2–4 Hz as a function of hypocentral distance. The simulated PEP_T with larger ε (0.07 and 0.09) shows an almost constant value irrespective of hypocentral distance. The composite model with $\varepsilon = 0.07$ successfully reproduced the observed PEP_T. Takemura & Furumura (2013) also used same parameters in simulation without topography, but their simulation was somewhat smaller than observation. The relative contributions of scattering due to velocity heterogeneity and topography are approximately 88 and 12 per cent, respectively.

The discrepancy at shorter distances may indicate that our FDM simulation still underestimates the scattering of high-frequency *P* waves, especially for shorter epicentral distances. This is likely due to the absence in the present simulation of near-surface low-velocity

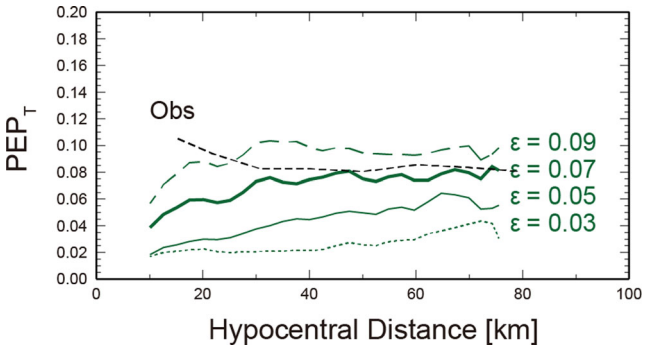

Figure 7. Changes in PEP_T as a function of hypocentral distance derived from simulation of the composite model with various rms values (ε). The dashed line represents the PEP_T of the observations of Takemura & Furumura (2013).

($V_S < 3.0$ km s^{-1}) sedimentary layers with rich shorter-wavelength heterogeneities. To resolve this circumstance, we would need to evaluate such an additional effect on the scattering of the high-frequency wavefield using very detailed near-surface structure and a high-performance computer when these are available in the future.

2.3 Simulation of scattered *S* waves

We then examined the distortion of the apparent *S*-wave radiation pattern caused by seismic wave scattering based on the 3-D FDM simulation of seismic wave propagation in heterogeneous structure. The term 'apparent radiation pattern' indicates the amplitude distribution pattern, which includes source, path and site effects. On the other hand, the term 'original source radiation pattern' indicates the amplitude pattern expected by a double-couple point dislocation, including only the source effect.

Takemura *et al.* (2009) conducted 2-D FDM simulations using a velocity inhomogeneity model. Here, we revisit our former study by employing 3-D FDM simulations to examine the relative contributions of irregular topography and velocity inhomogeneity, which distort the apparent *S*-wave radiation pattern.

Fig. 8 displays snapshots of seismic wave propagation derived from the 3-D FDM simulation with a strike-slip-fault point source ($Mxy = 1.0$) located in the centre of the FDM model at a depth of 5 km below the surface. Seismic moment and source time function were same as previous simulations of *P* wave source. It shows a spread of the four-lobe amplitude distribution pattern of the *P* and *S* waves radiating from the source at the earlier time frames. As the seismic wave propagates in the heterogeneous structure, the apparent radiation pattern for the *P* and *S* waves distorts gradually from the original four-lobe source radiation pattern, constructing almost isotropic distributions for all directions and following the long-duration *S*-wave coda.

In the irregular topography model (Fig. 8a), the apparent radiation pattern mostly preserves the original four-lobe source radiation pattern for *P* and *S* waves, even propagating for longer distances. However, the distortion of the apparent radiation pattern of the velocity inhomogeneity model is very significant for even short-distance propagation, showing an almost isotropic distribution of *S*-wave amplitudes for all directions at the later time frame ($t = 18$ s, Fig. 8b). The snapshot of the composite model (Fig. 8c) demonstrates a more realistic scattered seismic wavefield with large and long-duration *S* wave and distorted apparent *P*- and *S*-wave radiation pattern from the original four-lobe source radiation pattern caused by seismic wave scattering due to the irregular topography and velocity inhomogeneity.

2.4 Distortion of the apparent *S*-wave radiation pattern

In order to quantify the strength of the distortion of the apparent *S*-wave radiation pattern, we calculated the correlation coefficient (CC) between the simulated apparent *S*-wave radiation pattern and the theoretical expectation for a double-couple point dislocation.

Fig. 9 shows the relative strength of the *S* wave in the transverse component (hereafter denoted as A_T) compared to the vector composition of the horizontal components as a function of the azimuth measured from the fault strike:

$$A_T(\phi_i) = \frac{|T_{\max}(\phi_i)|}{\sqrt{[R_{\max}(\phi_i)]^2 + [R_{\max}(\phi_i)]^2}}, \quad (2)$$

where ϕ_i is the azimuth of *i*th station from fault-strike direction and $R_{\max}$ and $T_{\max}$ are the maximum *S*-wave amplitudes of the radial and transverse components, respectively. We compared A_T distributions for the frequencies of 0.5 and 4 Hz (Fig. 9), which were calculated from the maximum amplitudes of the horizontal waveforms recorded at stations at hypocentral distance of 20–60 km. The expected distribution of A_T for the strike-slip-fault source in a homogeneous medium (Aki & Richards 2002) is also illustrated in Fig. 9 by the dashed lines.

The simulation results show that the distributions of simulated A_T for the low frequency ($f = 0.5$ Hz; Figs 9a–c) preserve the original four-lobe *S*-wave source radiation pattern with larger A_T in the direction of fault strike and its normal directions. Even though the distortion of the apparent *S*-wave radiation pattern is rather strong at the high frequency ($f = 4$ Hz), the four-lobe pattern is almost preserved in the irregular topography model (Fig. 9d).

However, for the high frequency, the distortion of the A_T distribution pattern of the velocity inhomogeneity model is very strong, showing an almost isotropic A_T distribution for all directions (Fig. 9e). Therefore, the distortion of the apparent *S*-wave radiation pattern and homogenization of the seismic energy for all directions is considered to be caused mostly by the seismic wave scattering due to velocity inhomogeneity in the subsurface structure.

Fig. 10 shows the change in the CC between the simulated A_T pattern and the theoretical expectation as a function of hypocentral distance (Fig. 10a) and frequency (Fig. 10b) with the estimation errors evaluated by the bootstrap method (Efron & Tibshirani 1986). The figure shows that the original four-lobe shape of the *S*-wave source radiation pattern becomes distorted very rapidly as the seismic wave spreads from a source with distance over $D = 20$ km, with a decrease of CC from 0.8 to 0.6 at hypocentral distance between 20 and 45 km. The contribution of the topographic scattering to the distortion of the apparent radiation pattern is very weak, as shown by the larger CC value from 0.95 to 0.9 over the same distance range. Capdeville *et al.* (2010) pointed out that the apparent radiation pattern is distorted by energy conversion due to heterogeneities near seismic source. In our results (Fig. 10a), we also confirmed that distortion due to velocity inhomogeneities was stronger than that due to irregular topography even for distance less than 20 km. The composite model gave a significant reduction in CC, from 0.9 to 0.5 in hypocentral distances from 10 to 45 km. The strength of the CC derived by the present 3-D FDM simulation is somewhat larger than that observed in southwestern Japan (dashed line in Fig. 10a; Takemura *et al.* 2009).

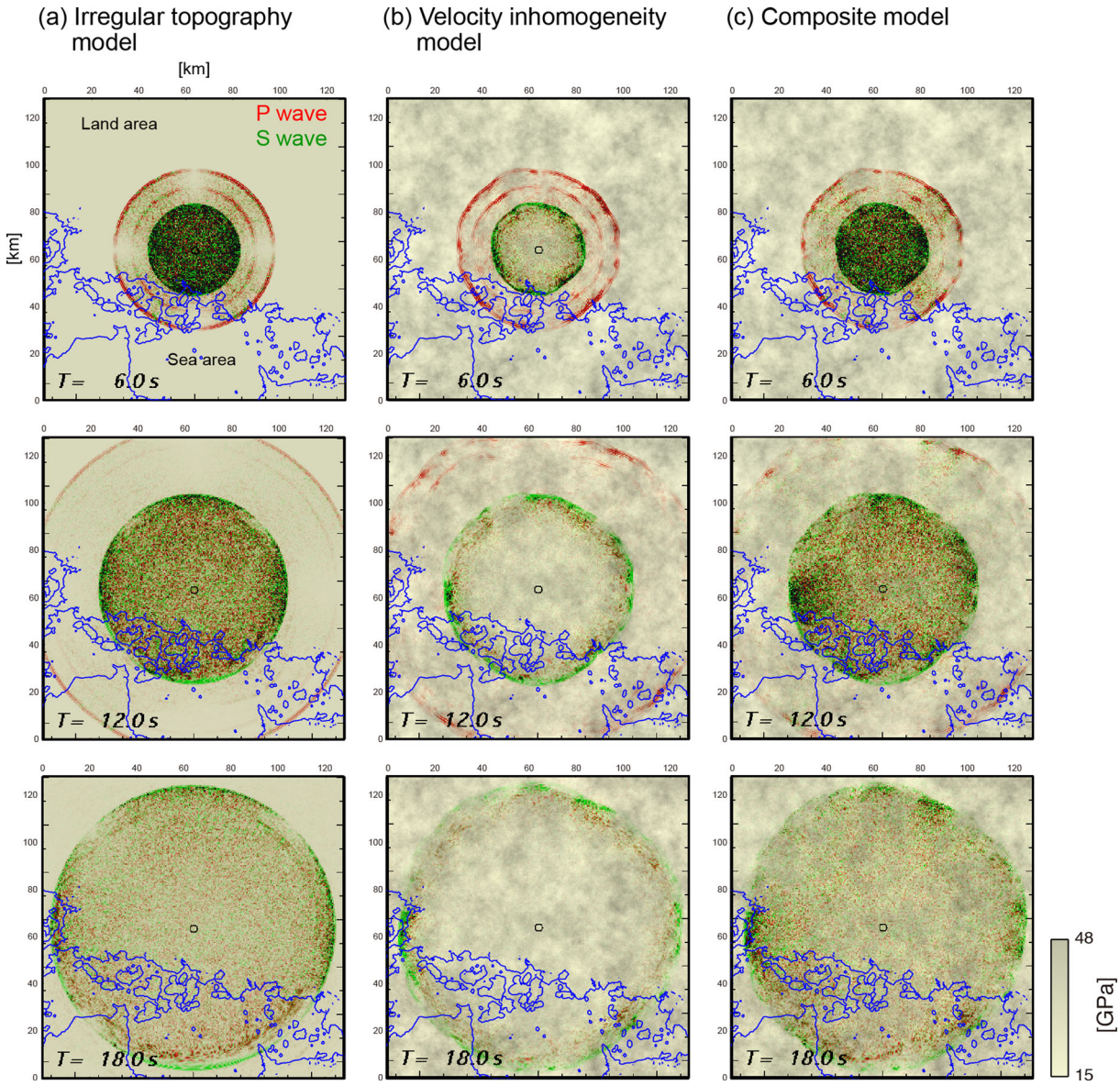

Figure 8. Snapshots of the seismic wavefield at the surface at $t = 6$, 12 and 18 s from the earthquake origin time showing the radiation of P (red) and S (green) waves from a strike-slip-fault source derived from the simulation results of (a) the irregular topography model, (b) the velocity inhomogeneity model and (c) the composite model including both velocity inhomogeneity and irregular topography.

Fig. 10(b) illustrates the decrease in the CC as a function of frequency ($f = 0.75$–4 Hz) derived from the simulation at distances of 20–60 km, demonstrating a reduction of CC with increasing frequency for both heterogeneous models. The decay curve of the CC for the composite model with increasing frequency is similar to that of the observation of Takemura *et al.* (2009), but the simulation results show larger CC than the observation. Although the observed CC for each frequency is an average value of data with a wider distance range of 10–100 km, the larger CC of the simulation probably occurred because our present simulation model is still too simple to fully explain the actual scattering seismic wavefield. To overcome this problem in future research, we should consider effects due to disregarding near-surface sedimentary layers and irregularities of crustal interfaces.

Fig. 11 shows the change in the CC derived from the simulations of the composite model with variation of the rms values of velocity fluctuations ($\varepsilon = 0.03$, 0.05, 0.07 and 0.09). The figure shows that CC for the larger ε values ($= 0.07$ and 0.09) decreases very quickly with increasing distance.

By comparison between simulations and observations, the small-scale velocity inhomogeneity model, which is characterized by the von Kármán PSDF with $a = 5$ km, $\varepsilon = 0.07$ and $\kappa = 0.5$, can well explain the frequency and distance dependencies of the observed P-wave polarization and apparent S-wave radiation patterns.

3 REGIONAL DIFFERENCE IN THE STRENGTH OF TOPOGRAPHIC SCATTERING

In the previous section, we examined the strength of scattering of high-frequency P and S waves propagating in the irregular topography model of southwestern Japan. As we noted earlier, the topographic scattering is a local effect around each station, thus the characteristics of the topographic scattering would be different in

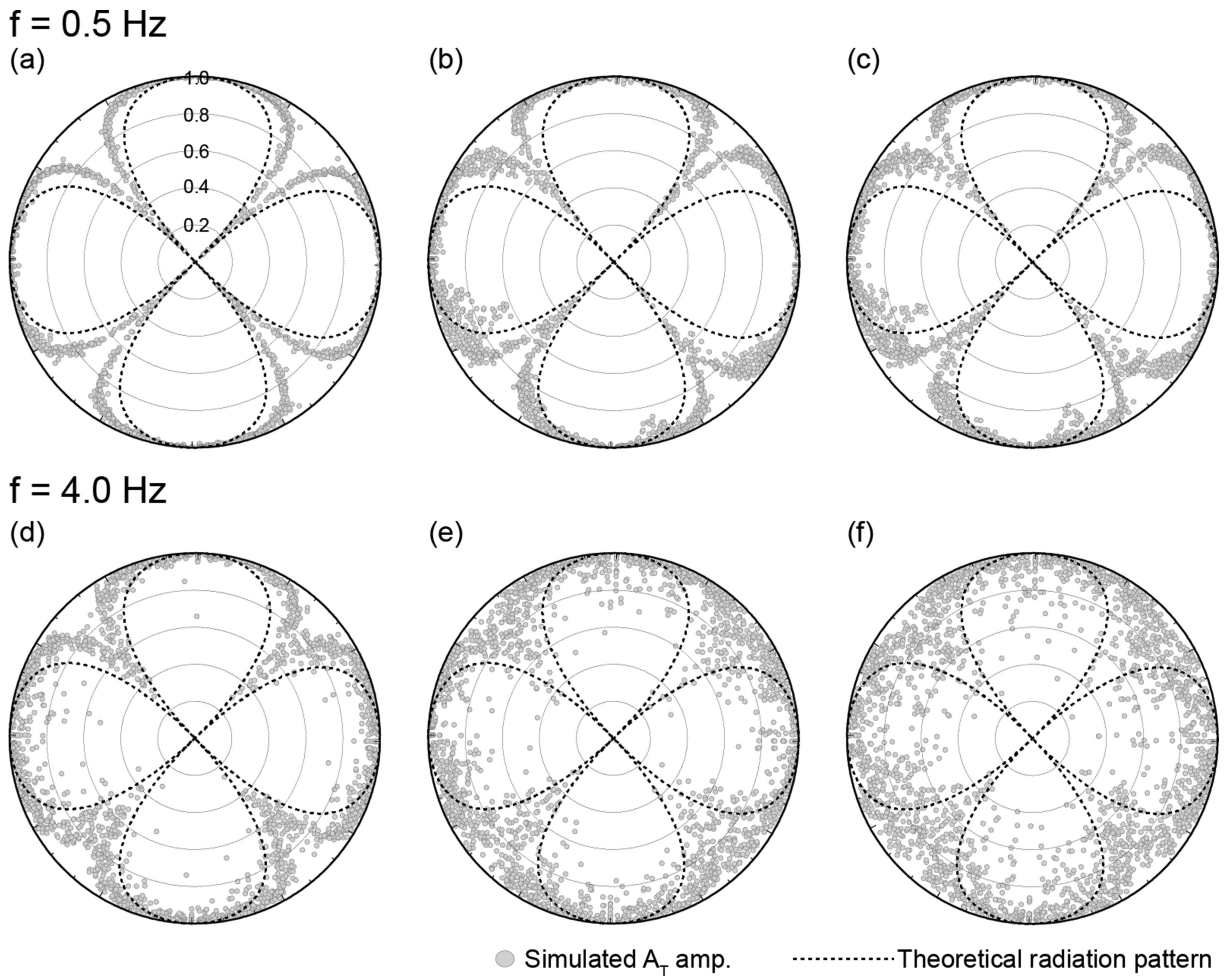

Figure 9. Distribution of relative transverse component amplitude A_T as a function of azimuth from fault strike obtained from simulation results for frequencies of $f = 0.5$ Hz and $f = 4$ Hz using (a, d) the irregular topography model, (b, e) the velocity inhomogeneity model and (c, f) the composite model including both velocity inhomogeneity and irregular topography. The grey dots represent the amplitudes of the *T* components of the simulated *S*-waves relative to the rms amplitudes of the horizontal components. The theoretical radiation pattern for *SH* waves in a homogeneous medium (Aki & Richards 2002) is represented by broken lines.

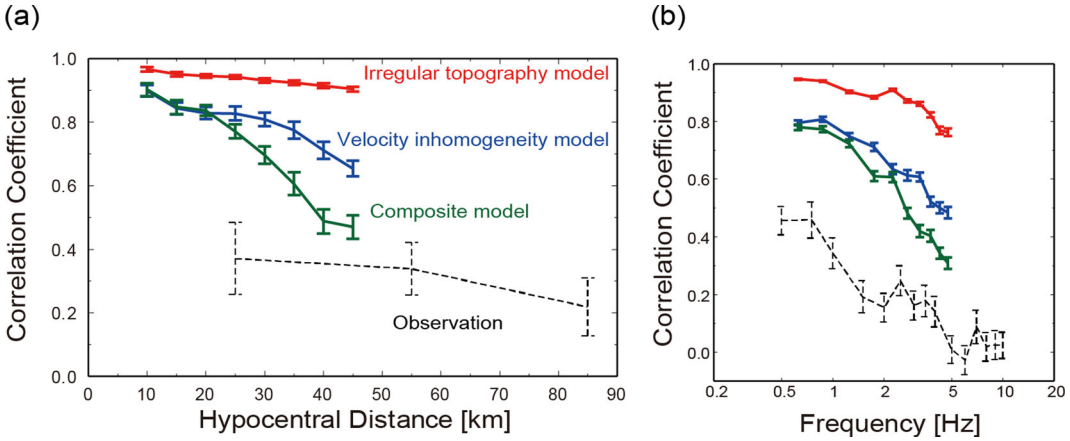

Figure 10. Correlation coefficients for the spatial distribution of A_T between the theoretical *SH* wave radiation pattern and the results of 3-D FDM simulations using the irregular topography model (red line), the velocity inhomogeneity model (blue line) and the composite model including both velocity inhomogeneity and irregular topography (green line) as a function of (a) hypocentral distance and (b) frequency. Dashed lines denote the observations of Takemura *et al.* (2009).

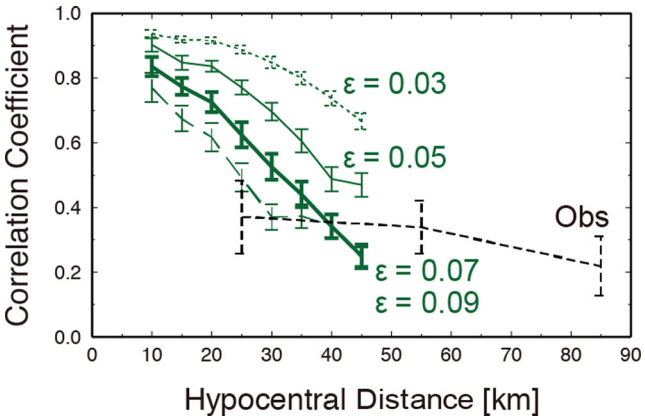

Figure 11. Correlation coefficients for the spatial distribution of A_T between the theoretical *SH* wave radiation pattern and the results of 3-D FDM simulations of the composite model with various rms values (ε) as a function of hypocentral distance. Dashed lines denote that of observations of Takemura *et al.* (2009).

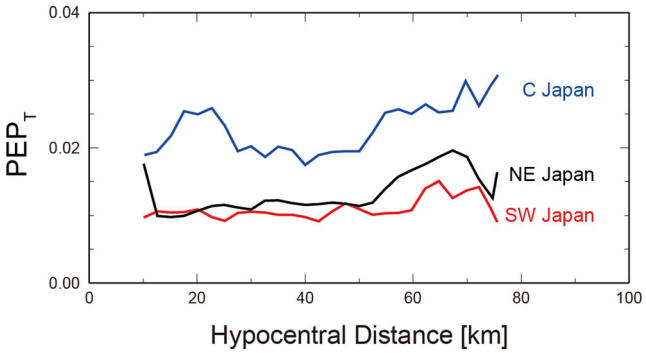

Figure 13. Change in PEP_T as a function of distance for frequencies of 2–4 Hz derived from the 3-D FDM simulation using the irregular topography model for southwestern (red line), central (blue line) and northeastern (back line) Japan.

each region of Japan with different features of topographic variation. To examine the strength of the topographic scattering properties expected from regional variation of topographies in different regions, we compared with the spectrums of the surface topographies in central Japan and northern Japan.

We first calculated the 1-D power spectral density (PSD) $P(k)$ along each horizontal (x, y) direction of the model region:

$$P(k) = \int_{-\infty}^{\infty} \delta h(x)\ \exp(\mathrm{i}kx)\,\mathrm{d}x, \tag{3}$$

where $\delta h\ (x)$ is the surface elevation from mean sea level, k is the wavenumber and dx is the horizontal grid interval of the model. We then averaged the value of each 1-D $P(k)$ for the x and y directions, assuming $V_S = 3.36\,\mathrm{km\ s^{-1}}$ and $f = V_S\ k/2\pi$ (Fig. 12). It was confirmed that all PSDs for the three regions show power-law decay with increasing wavenumber. The shapes of the PSDs are explained well by the von Kármán-type PSDF rather than the Gaussian PSDF, which has a band-limited property of the spectrum. This means that the surface topography is characterized by various scales of heterogeneities, similar to the distribution of small-scale velocity inhomogeneity in the crust and mantle. Similar observations were also reported by Kumagai *et al.* (2011), who examined the spectrum of the complex volcanic topography at Mt Cotopaxi, Ecuador.

We also found that the topographic irregularities of northeastern Japan were almost as strong as those of southwestern Japan and had similar PSD, whereas the strength of the PSD of the topographic variation in central Japan was twice as large as that of southwestern Japan due to the existence of tall mountains (>2500 m) and deep sea (<−1000 m) in this region.

We compared the effects of topographic scattering in central, northeastern and southwestern Japan through 3-D FDM simulation of seismic wave propagation by examining the value of the PEP_T (Fig. 13) and CC of the apparent *S*-wave radiation pattern (Fig. 14). The simulation results confirmed an approximately twice larger topographic scattering in central Japan than in southwestern or northeastern Japan, and the value is almost unchanged for all distances. The unchanging feature of PEP_T in all regions supports our conclusion that the topographic scattering does not accumulate with increasing distance and is a local effect around each station.

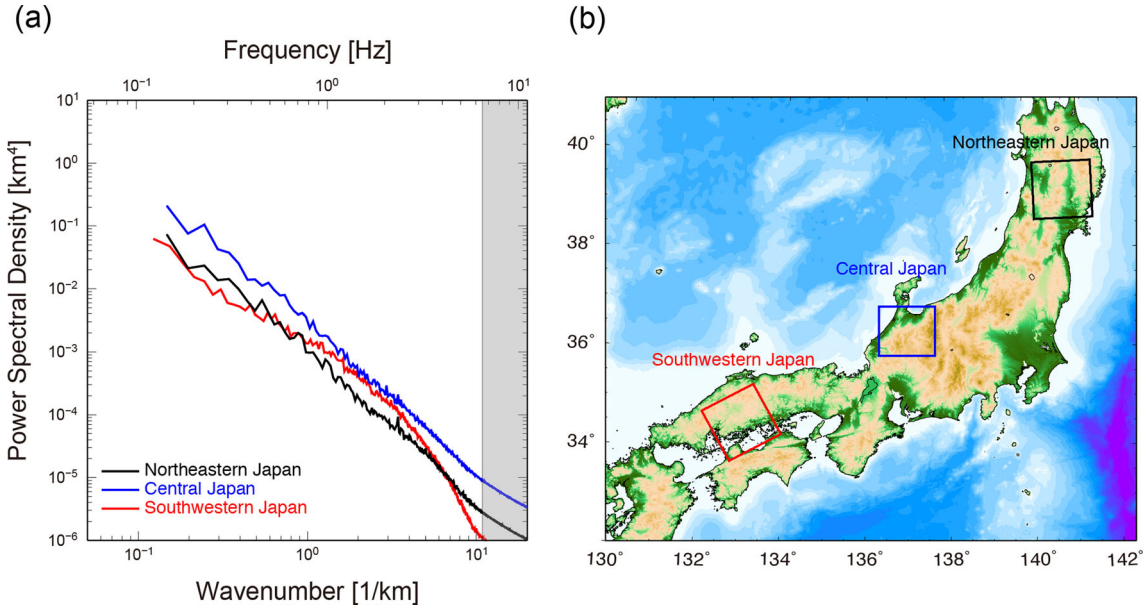

Figure 12. Comparison of the averaged 1-D power spectral density (PSD) of ground elevation for southwestern (red line), central (blue line) and northeastern (black line) Japan.

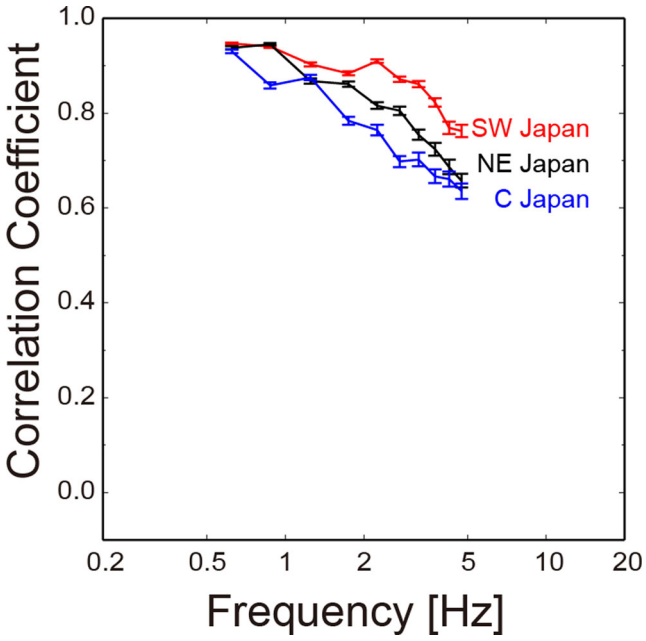

Figure 14. Changes in the correlation coefficient as a function of frequency for the spatial distribution of A_T: correlation between the theoretical *SH* wave radiation pattern and FDM simulations using the irregular topography model for southwestern (SW; red line), central (C; blue line) and northeastern (NE; back line) Japan.

We also confirmed that the distortion of the apparent *S*-wave radiation pattern in central Japan is much stronger in central Japan, especially for higher frequencies. The relative strength of the topographic scattering does depend on the topography of each region, so it is easily estimated in advance by spectral analysis of elevation data.

In previous studies, the scattering of high-frequency seismic waves was often explained by small-scale velocity inhomogeneity in the subsurface structure alone. Thus, the estimated small-scale velocity inhomogeneities (especially ε) and the energy of seismic wave scattering based on conventional analysis methods, such as *P*-wave polarization (e.g. Kubanza *et al.* 2007; Nishimura 2012; Takemura & Furumura 2013), the apparent *S*-wave radiation pattern (e.g. Takemura *et al.* 2009; Sawazaki *et al.* 2011) and coda energy measurements (e.g. Fehler *et al.* 1992; Hoshiba 1993; Carcole & Sato 2010), might be overestimated because effects of irregular topography are not considered. Therefore, we may need to evaluate the effects of irregular topography in addition to the effects of velocity inhomogeneity to model a realistic high-frequency scattering wavefield and for precise estimation of the strength of the velocity inhomogeneity by comparing simulation and observation.

4 CONCLUSIONS

In this study, we examined the effects of irregular topography and small-scale velocity inhomogeneity on high-frequency seismic wave propagation by 3-D FDM simulations using realistic topography and stochastic velocity inhomogeneity models for crustal earthquakes of southwestern Japan and compared with observations derived by our previous studies (Takemura *et al.* 2009; Takemura & Furumura 2013). We especially examined the *P*-wave polarization pattern, the apparent *S*-wave radiation pattern and coda waves (scattered body waves) for shallow crustal earthquakes.

The results demonstrated that the scatterings of body waves due to topography and velocity inhomogeneity show completely different properties. Topographic scatterings of body waves have only localized effects that occur when direct *P* and *S* waves arrive at the surface. This effect does not accumulate as seismic waves propagate. On the other hand, seismic wave scattering due to small-scale velocity inhomogeneity in the subsurface structure causes a much stronger effect for modifying *P*- and *S*-wave propagation features. Moreover, these effects accumulate gradually with propagation. By comparisons between simulations and observations for *P* and *S* waves, it was estimated that the small-scale velocity heterogeneity in the crust of southwestern Japan can be modelled by the von Kármán PSDF with $a = 5$ km, $\varepsilon = 0.07$ and $\kappa = 0.5$. The relative strengths of the scattering of body waves due to velocity heterogeneity and irregular topography in southwestern Japan are approximately 88 and 12 per cent, respectively. These values may depend strongly on the topography of each region and can be roughly expected by using spectral analysis.

The results of our study indicate that for modelling of the high-frequency seismic wavefield, such considerations of irregular surface topography and small-scale velocity inhomogeneity should be considered fully in the model, which yields a realistic seismic wavefield such as associating long coda, modifying polarizations of the seismic energy in three-component seismograms, and distorting and homogenizing the apparent *P*- and *S*-wave radiation patterns for all directions, as we saw in actual high-frequency seismograms.

ACKNOWLEDGEMENTS

We thank Dr O'Brien, an anonymous reviewer, and the editor, Dr E. Fukuyama, for constructive comments that improved an earlier draft of this manuscript. We acknowledge the National Research Institute for Earth Science and Disaster Prevention (NIED) in Japan for providing the K-NET/KiK-net and Hi-net waveform data. The FDM simulations were conducted on the Earth Simulator at the Japan Agency for Marine-Earth Science and Technology (JAMSTEC) under the support of a joint research project between the Earthquake Research Institute, the University of Tokyo, and the Earth Simulator Center entitled 'Seismic wave propagation and strong ground motion in 3-D heterogeneous structure.' We are grateful for financial support in the form of Grants-in-Aid for the Japan Society for the Promotion of Science fellows (Grant Nos 21.3509 and 24.5704). The figures were created using the Generic Mapping Tools (GMT) software package developed by Wessel & Smith (1998). This research was part of the PhD thesis of ST (Takemura 2012, chapters 4 and 5).

REFERENCES

Aki, K. & Chouet, B., 1975. Origin of coda waves: source, attenuation, and scattering effects, *J. geophys. Res.,* **80,** 3322–3342.

Aki, K. & Richards, P., 2002. *Quantitative Seismology,* 2nd edn, University Science Books.

Birch, A.F., 1961. The velocity of compressional waves in rocks to 10 kilobars, part 2, *J. geophys. Res.,* **66,** 2199–2224.

Capdeville, Y. & Marigo, J.J., 2013. A non-periodic two scale asymptotic method to take account of rough topographies for 2-D elastic wave propagation, *Geophys. J. Int.,* **192,** 163–189.

Capdeville, Y., Guillot, L. & Marigo, J.J., 2010. 2D non-periodic homogenization to upscale elastic media for P-SV waves, *Geophys. J. Int.,* **182,** 903–922.

Carcole, E. & Sato, H., 2010. Spatial distribution of scattering loss and intrinsic absorption of short-period *S* waves in the lithosphere of Japan on the basis of the Multiple Lapse Time Window Analysis of Hi-net data, *Geophys. J. Int.,* **180,** 268–290.

Efron, B. & Tibshirani, R., 1986. Bootstrap methods for standard errors, confidence intervals, and other measures of statistical accuracy, *Stat. Sci.,* **1**(1), 54–77.

Fehler, M., Hoshiba, M., Sato, H. & Obara, K., 1992. Separation of scattering and intrinsic attenuation for the Kanto-Tokai region, Japan, using measurements of *S*-wave energy versus hypocentral distance, *Geophys. J. Int.,* **108,** 787–800.

Hayashi, K., Burns, D.R. & Toksoz, M.N., 2001. Discontinuous-grid finite-difference seismic modeling including surface topography, *Bull. seism. Soc. Am.,* **91,** 1750–1764.

Hoshiba, M., 1993. Separation of scattering attenuation and intrinsic absorption in Japan using the multiple lapse time window analysis of full seismogram envelope, *J. geophys. Res.,* **98,** 15 809–15 824.

Imperatori, W. & Mai, P.M., 2013. Broad-band near-field ground motion simulations in 3-dimensional scattering media, *Geophys. J. Int.,* **192,** 725–744.

Kinoshita, S., 1998. Kyoshin Net (K-NET), *Seism. Res. Lett.,* **69,** 302–332.

Köhler, A., Weidle, C. & Maupin, V., 2012. On the effect of topography on surface wave propagation in the ambient noise frequency range, *J. Seismol.,* **16,** 221–231.

Kubanza, M., Nishimura, T. & Sato, H., 2007. Evaluation of strength of heterogeneity in the lithosphere from peak amplitude analysis of teleseismic short-period P waves, *Geophys. J. Int.,* **171,** 390–398.

Kumagai, H., Saito, T., O'Brien, G. & Yamashina, T., 2011. Characterization of scattered seismic wavefields simulated in heterogeneous media with topography, *J. geophys. Res.,* **116,** B03308, doi:10.1029/2010JB007718.

Liu, H. & Helmberger, D.V., 1985. The 23:19 aftershock of the 15 October 1979 Imperial valley earthquake: more evidence for an asperity, *Bull. seism. Soc. Am.,* **75,** 689–708.

Maeda, T. & Furumura, T., 2013. FDM simulation of seismic waves, ocean acoustic waves, tsunami based on tsunami-coupled equations of motion, *Pure. appl. Geophys.,* **170,** 109–127.

Maradudin, A.A., Haung, X. & Mayer, A.P., 1991. Propagation of shear horizontal surface acoustic waves parallel to the grooves of a random grating, *J. appl. Phys.,* **70,** 53–62.

Mavroeidis, G.P. & Papageorgiou, A.S., 2003. A mathematical representation of near-field ground motions, *Bull. seism. Soc. Am.,* **93,** 1099–1131.

Mayer, A.P., Zierau, W. & Maradudin, A.A., 1991. Surface acoustic waves propagating along the grooves of a periodic grating, *J. appl. Phys.,* **69,** 1942–1947.

Nakamura, T., Takenaka, H., Okamoto, T. & Kaneda, Y., 2012. FDM simulation of seismic wave propagation for an aftershock of the 2009 Suruga Bay earthquake: effects of ocean-bottom topography and seawater layer, *Bull. seism. Soc. Am.,* **102,** 2420–2435.

Nielsen, L., Thybo, H., Levander, A. & Solodilov, L.N., 2003. Origin of upper-mantle seismic scattering—evidence from Russian peaceful nuclear explosion data, *Geophys. J. Int.,* **154,** 196–204.

Nishimura, T., 2012. Heterogeneity of the Japan islands as inferred from transverse component analysis of teleseismic P-waves observed at a seismic station network, Hi-net, *Earth Planets Space,* **64,** e25–e28.

O'Brien, G. & Bean, C., 2009. Volcano topography, structure and intrinsic attenuation: their relative influences on a simulated 3D visco-elastic wavefield, *J. Volc. Geotherm. Res.,* **183,** 122–136.

Obara, K., Kasahara, K., Hori, S. & Okada, Y., 2005. A densely distributed high-sensitivity seismograph network in Japan: Hi-net by National Research Institute for Earth Science and Disaster Prevention, *Rev. Sci. Instrum.,* **76,** 021301, doi:10.1063/1.1854197.

Ohminato, T. & Chouet, B., 1997. A free-surface boundary condition for including 3D topography in the finite difference method, *Bull. seism. Soc. Am.,* **87,** 494–515.

Okada, Y., Kasahara, K., Hori, S., Obara, K., Sekiguchi, S., Fujiwara, H. & Yamamoto, A., 2004. Recent progress of seismic observation networks in Japan—Hi-net, F-net, K-NET and KiK-net, *Earth Planets Space,* **56,** xv–xxviii.

Okamoto, T. & Takenaka, H., 2005. Fluid-solid boundary implementation in the velocity-stress finite-difference method, *Zisin 2,* **57,** 355–364 (in Japanese with English abstract).

Przybilla, J., Korn, M. & Wegler, U., 2006. Radiative transfer of elastic waves versus finite difference simulations in two-dimensional random media, *J. geophys. Res.,* **111,** B04305, doi:10.1029/2005JB003952.

Przybilla, J., Korn, M. & Wegler, U., 2009. Estimation of crustal scattering parameters with elastic radiative transfer theory, *Geophys. J. Int.,* **178,** 1105–1111.

Ripperger, J., Igel, H. & Wasserman, J., 2003. Seismic wave simulation in the presence of real volcano topography, *J. Volc. Geotherm. Res.,* **128,** 31–44.

Robertsson, J., 1994. Viscoelastic finite-difference modeling, *Geophysics,* **59,** 1444–1456.

Saito, T., Sato, H., Ohtake, M. & Obara, K., 2005. Unified explanation of envelope broadening and maximum-amplitude decay of high-frequency seismograms based on the envelope simulation using the Markov approximation: forearc side of the volcanic front in northeastern Honshu, Japan, *J. geophys. Res.,* **110,** B01304, doi:10.1029/2004JB003225.

Sato, H., 1984. Attenuation and envelope formation of three-component seismograms of small local earthquakes in randomly inhomogeneous lithosphere, *J. geophys. Res.,* **89,** 1221–1241.

Sato, H., 1989. Broadening of seismogram envelopes in the randomly inhomogeneous lithosphere based on the parabolic approximation: southeastern Honshu, Japan, *J. geophys. Res.,* **94,** 17 735–17 747.

Sato, H., Fehler, M. & Maeda, T., 2012. *Seismic Wave Propagation and Scattering in the Heterogeneous Earth Structure,* 2nd edn, Springer-Verlag.

Sawazaki, K., Sato, H. & Nishimura, T., 2011. Envelope synthesis of short-period seismograms in 3-D random media for a point shear dislocation source based on forward scattering approximation: application to small strike-slip earthquakes in southwestern Japan, *J. geophys. Res.,* **116,** B08305, doi:10.1029/2010JB008182.

Takahashi, T., Sato, H., Nishimura, T. & Obara, K., 2007. Strong inhomogeneity beneath Quaternary volcanoes revealed from the peak delay analysis of S-wave seismograms of microearthquakes in northeastern Japan, *Geophys. J. Int.,* **168,** 90–99.

Takahashi, T., Sato, H., Nishimura, T. & Obara, K., 2009. Tomographic inversion of the peak delay times to reveal random velocity fluctuations in the lithosphere: method and application to northeastern Japan, *Geophys. J. Int.,* **178,** 1437–1455.

Takemura, S., 2012. Study of high-frequency seismic wave propagation in heterogeneous structure inferred from dense array observations and numerical simulations, *PhD thesis,* the University of Tokyo, Japan.

Takemura, S. & Furumura, T., 2013. Scattering of high-frequency *P* wavefield derived from by the dense Hi-net array observations in Japan and computer simulations of seismic wave propagations, *Geophys. J. Int.,* **193,** 421–436.

Takemura, S., Furumura, T. & Saito, T., 2009. Distortion of the apparent *S*-wave radiation pattern in the high-frequency wavefield: Tottori-ken Seibu, Japan, earthquake of 2000, *Geophys. J. Int.,* **178,** 950–961.

Wessel, P. & Smith, W.H.F., 1998. New improved version of generic mapping tools released, *EOS, Trans. Am. geophys. Un.,* **79**(47), 579, doi:10.1029/98EO00426.

APPENDIX A

Accuracy of FDM simulation with topography

We employed the air/solid boundary condition proposed by Okamoto & Takenaka (2005) to achieve precise FDM simulation of seismic wave propagation in the medium including irregular surface topography based on a staircase-shaped approximation of the free surface (e.g. Hayashi *et al.* 2001). This method explicitly uses a zero-shear stress boundary condition on the ground surface in addition to using second-order finite difference approximations to the grids around the free surface, which leads to successful application

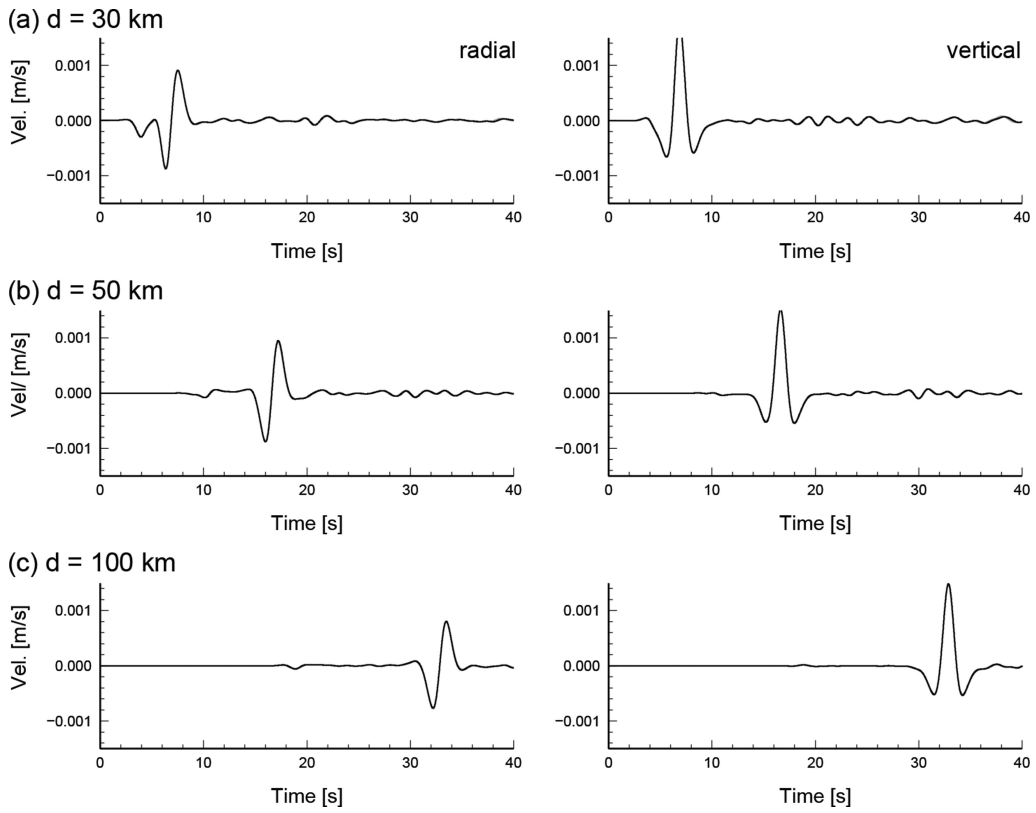

Figure A1. Comparison of synthetic waveforms between the basic (dx = 0.1) and finer (dx = 0.05) models at epicentral distances of d = 30, 50 and 100 km. A bandpass filter for the frequency band of f = 0.01–0.5 Hz was applied. Black and grey lines represent simulation results from the basic and finer models, respectively.

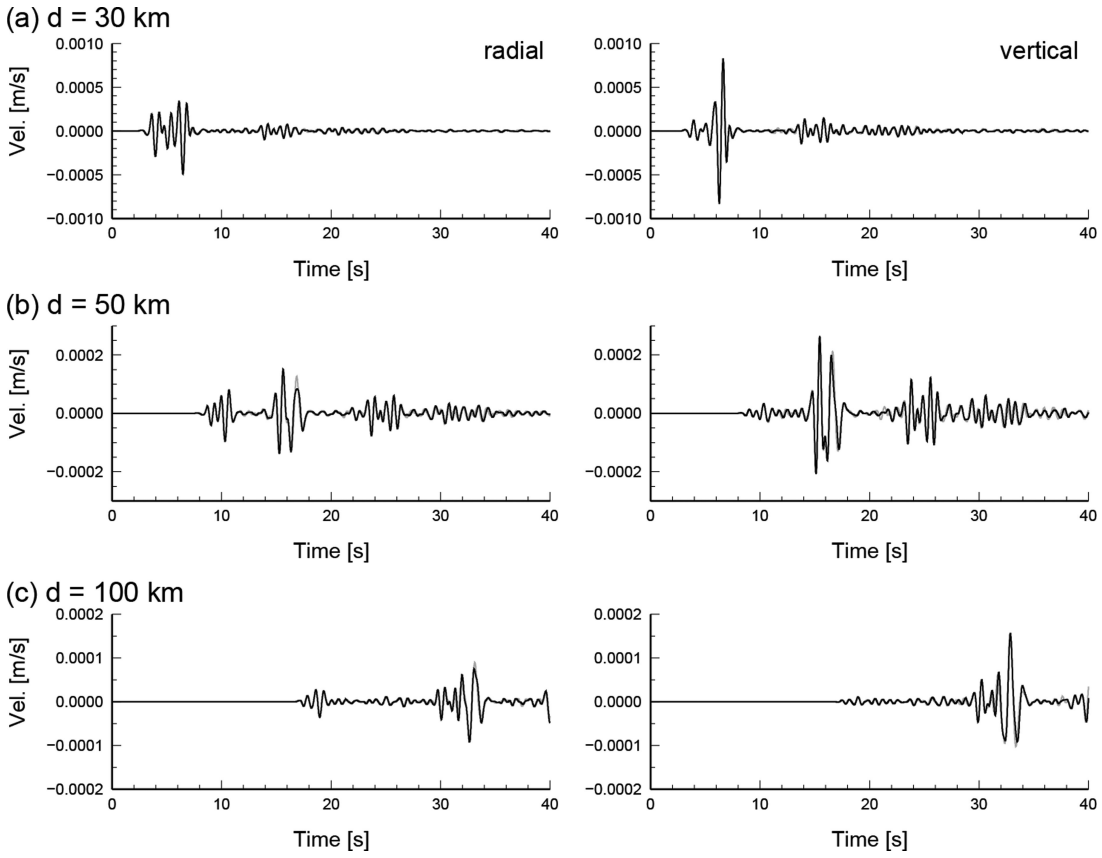

Figure A2. As in Fig. A1 but for high-frequency (f = 1–4 Hz) components.

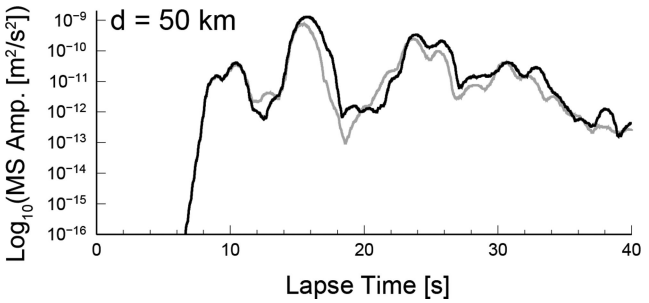

Figure A3. Comparison of *S*-coda envelope between the basic and finer models. A bandpass filter for the frequency band of 2–4 Hz was applied to all traces. Black and grey lines denote the MS envelopes derived from the basic and finer models, respectively.

under the realistic topography and bathymetry (e.g. Ohminato & Chouet 1997; Nakamura *et al.* 2012; Maeda & Furumura 2013). We confirmed the accuracy of our FDM scheme in 2-D space through a comparison of simulation results with different grid spacings.

Because our FDM scheme for irregular topography is second-order accurate in space, it is expected that the accuracy of the FDM simulation should improve with decreasing grid size. Therefore, we believed our finer model, which has a smaller grid size, to be a good reference for checking calculation accuracy. Thus, we compared simulated waveforms between our basic ($dx = 0.1$ km, $dz = 0.05$ km) and finer ($dx = 0.05$, $z = 0.025$) models. We employed a vertical-slip source ($M_{XZ} = 1.0$) at a depth of 5 km below the surface using a single-cycle Kupper wavelet source-time function with a moment release of $M_0 = 1.0 \times 10^{12}$ Nm and a dominant period of $T_0 = 0.16$ s. The background velocity structure was the same as that in previous simulations and the topography model was from profile A′–B′ in Fig. 1(a).

Fig. A1 compares the low-frequency ($f = 0.01$–0.5 Hz) waveforms derived from our FDM simulations and indicates good agreement between models for propagation over distances greater than 100 km. The waveforms for our basic and finer models continue to show good agreement even as frequency increases ($f = 1$–4 Hz; Fig. A2).

In our real-world analyses, we compared coda envelope shapes rather than waveforms to measure the strength of the seismic wave scattering. Therefore, we synthesized the MS envelope by summing two components (radial and vertical) at each station and compared the accuracy of energy propagation in the models. The envelopes were synthesized by the squared sums of the waveforms and their Hilbert transforms. The envelopes were smoothed with a time window that was twice the corner period. Fig. A3 illustrates the MS

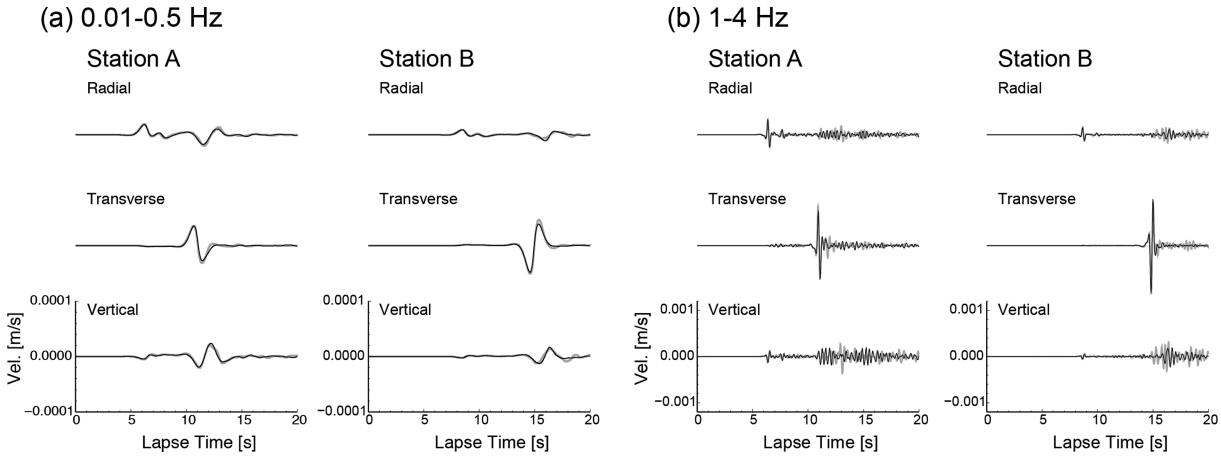

Figure A4. Comparison of three-component synthetic waveforms at stations A and B (see Fig. 1b) derived from the FDM simulation using a standard resolution model ($dx = 0.1$, $dz = 0.05$; black lines) and much finer ($dx = 0.05$, $dz = 0.05$; grey lines) model. A bandpass filter for the frequency band of $f = 0.01$–0.5 Hz was applied.

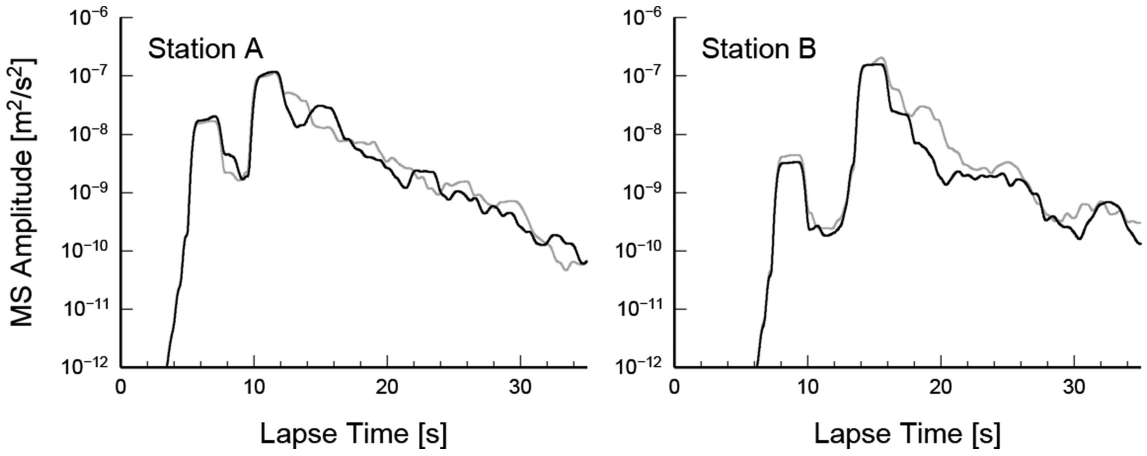

Figure A5. Comparison of *S*-coda envelope at stations A and B between the standard and the finer models. A bandpass filter for the frequency band of 2–4 Hz was applied to all traces.

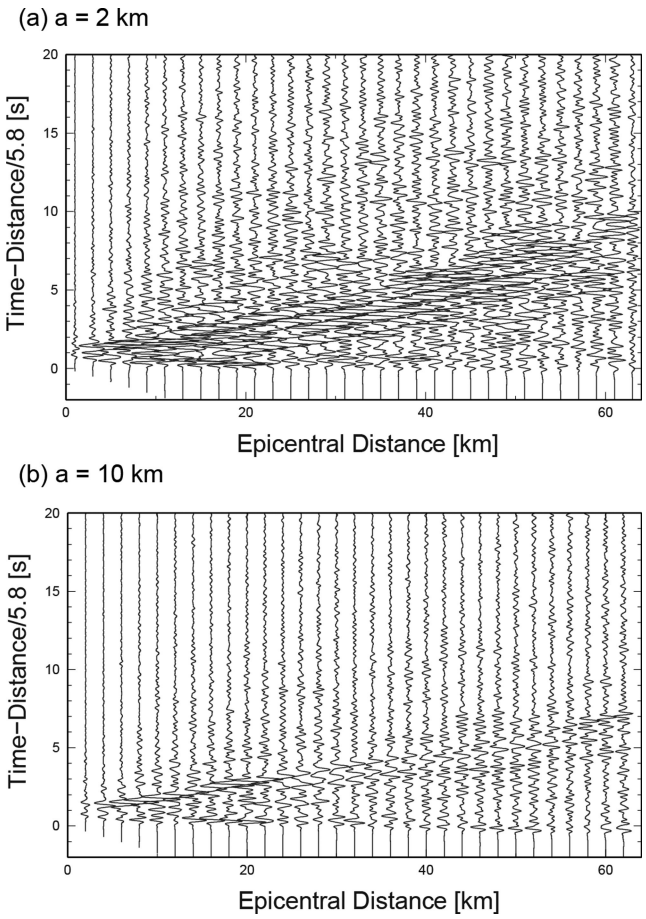

Figure B1. Synthetic seismograms of transverse-component ground velocity motion derived from the 3-D FDM simulation using the velocity inhomogeneity model with correlation distances of $a = 2$, 10 km. A bandpass filter for the frequency band $f = 1$–4 Hz was applied. Each trace was multiplied by the hypocentral distance to compensate for geometrical spreading of body waves.

envelopes obtained using both waveforms recorded at a hypocentral distance of 50 km. Our results demonstrated good agreement between models in terms of both direct wave amplitudes and decay of coda amplitudes (Fig. A3).

We also compared the results of 3-D simulations using a strike-slip source. Figs A4 and A5 show comparisons of waveforms between standard ($dx = dy = 0.1$ km, $dz = 0.05$ km) and finer ($dx = dy = dz = 0.05$) resolution models demonstrating good agreement between the two models in terms of amplitudes and decay of coda for high-frequency seismic waves.

Based on these comparisons in 2-D and 3-D media, we conclude that the accuracy of our FDM simulations was sufficient to discuss the scattering of high-frequency seismic waves due to irregular surface topography. Previous studies have claimed that 20–25 grids per wavelength are required to achieve precise simulation of topography effects on surface waves (e.g. Ohminato & Chouet 1997). In our study, however, we focused on the propagation features of high-frequency seismic waves, including coda waves, which are constructed by scattered body waves (e.g. Sato *et al.* 2012, chapter 3). Furthermore, surface waves of such higher-frequency components are relatively weak compared to scattered body wave. Thus, we considered that the wavelength condition for high-frequency body waves might not be severe compared with the simulation of surface wave propagation. This was also supported by the results of the numerical experiments in this section.

APPENDIX B

Variations in waveforms due to the scattering of seismic waves in heterogeneous structure with different correlation distances ($a =$ 2 and 10 km) are compared in Fig. B1 with a record section of the transverse-component seismogram which is compared with Fig. 3(b) for the velocity inhomogeneity model with $a = 5$ km. It is clear that amplitude variation between stations is very strong in the record section of shorter correlation distance ($a = 2$ km) of heterogeneities compared with that for longer correlation distance ($a = 10$ km). The burst of P waveform amplitude observed in the transverse-component record section shown in Fig. 3b yields the correlation distance of the velocity inhomogeneity.

The waveform similarities between neighbouring stations as a function of lag distance between stations is shown in Fig. B2, which demonstrates that the decay of CCC with increasing lag distance is very strong, even for shorter lag distances, for the heterogeneity model with smaller a.

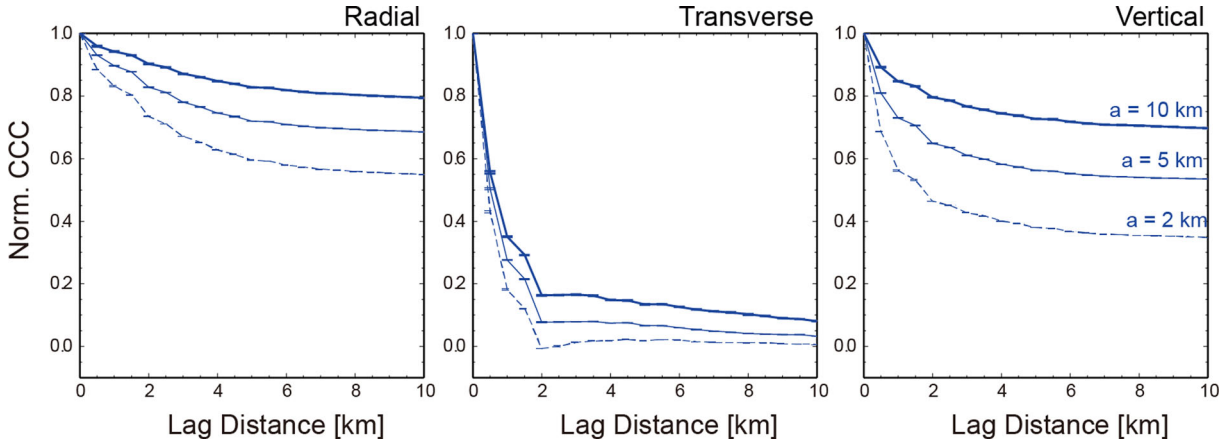

Figure B2. Change with distance in the cross-correlation coefficient (CCC) between station pairs: comparison between the velocity inhomogeneity model with various correlation distances ($a = 2$, 5 and 10 km). A bandpass filter for the frequency band of $f = 1$–4 Hz was applied. The cross-correlation coefficient was calculated by the P waveform for the 5-s time window that starts from P-wave arrival.